Graphical Abstract

Modulation of Optical and Electrical Properties of Amorphous Manganese Oxide Films: Effect of Oxygen Content

Y Makoudi*, C Rousselot, W Hourani*

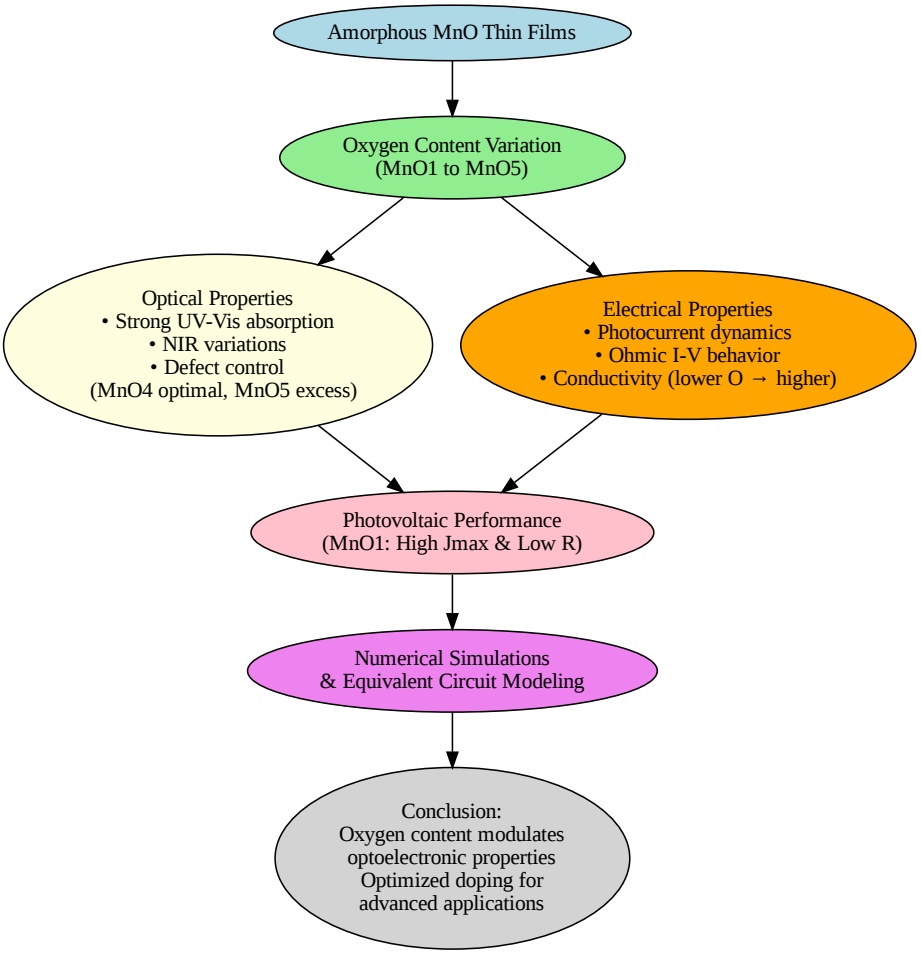

Highlights

Modulation of Optical and Electrical Properties of Amorphous Manganese Oxide Films: Effect of Oxygen Content

Y Makoudi*, C Rousselot, W Hourani*

- Research highlight 1
- Research highlight 2

Modulation of Optical and Electrical Properties of Amorphous Manganese Oxide Films: Effect of Oxygen Content

Y Makoudi*, C Rousselot, W Hourani*

Université Marie et Louis Pasteur, CNRS, Institut FEMTO-ST, Montbéliard, 25200, France

Abstract

This study investigates the optical, electrical, and photoelectric properties of amorphous MnO_x thin filmsdeposited via DC magnetron sputtering with varying oxygen flow rates. UV-Vis spectroscopy characterized the optical properties, current-voltage (I-V) characteristics revealed ohmic behavior, and photocurrent measurements responses demonstrated that optimal oxygen flow rate enhanced transparency and carrier generation, whereas excess oxygen introduced structural defects. Numerical simulations modeled the photocurrent behavior, providing insights for material optimization. The results demonstrate the potential of MnO_x films for applications in optoelectronics.

Keywords: MnO, thin films, PVD, oxygen flow rate, optoelectronics, amorphous, photocurrent, numerical simulation

1. Introduction

Transition metal oxides continue to attract significant scientific interest due to their intriguing physical and chemical properties[1]. Manganese oxide (MnO_x, where x represents the oxygen-to-manganese ratio) stands out for its natural abundance, low cost, and potential applications in diverse fields such as energy storage, catalysis, sensors, and optoelectronics [2, 3].

Numerous techniques have been developed for synthesizing manganese oxide thin films, each offering specific advantages. These include chemical vapor deposition (CVD) [4], radio-frequency (RF) sputtering [5], electrostatic spray deposition (ESD) [6], potentiostatic electrolysis, spray pyrolysis,

oblique angle deposition (OAD) [7], thermal evaporation, and pulsed laser deposition (PLD) [8]. The choice of deposition technique directly impacts the crystalline structure, stoichiometry, and resulting properties of MnO_x thin films.

A wide range of analytical techniques is employed to characterize these layers. Microscopy methods (optical[9],atomic force microscopy (AFM) [10], field-emission scanning electron microscopy (FESEM) [11], transmission electron microscopy (TEM) [12]) reveal morphology and structure at the nanoscale. Spectroscopic methods (Raman [9], X-ray photoelectron spectroscopy (XPS) [13], ultraviolet photoelectron spectroscopy (UPS) [9], ultraviolet-visible spectroscopy (UV-Vis) [3], Fourier-transform infrared spectroscopy (FTIR) [10], Rutherford backscattering spectrometry (RBS) [10]) provide information on chemical composition, bonding, and optical properties. X-ray diffraction (XRD) [3] is used for crystal structure analysis. Electrical measurements, such as the Van der Pauw [14] method and the Hall effect [11], characterize electronic transport properties.

Previous research has demonstrated the potential of crystalline manganese oxide forms, particularly α-MnO_2. Nanofilms of α-MnO_2 prepared by thermal evaporation show promise for heterojunction photodiodes [3], with structural, optical, and photoelectric properties suitable for solar energy conversion. Additional studies have reported MnO_2 films in supercapacitors and lithium-ion batteries, as well as Mn-ZnO photoanodes for photoelectrochemical water splitting [15]. Perovskites such as $RMnO_3$ ($R = \mathrm{Y, Er, and Yb}$) have been proposed for their small band gaps and potential in solar cells [11]. The influence of manganese doping on $CuInSe_2$ films has also been investigated [16].

However, these works primarily focus on crystalline MnO_2 thin films, while the properties of amorphous MnO_x thin films, particularly their optoelectronic characteristics, remain largely unexplored.

Compared to other amorphous transition metal oxides such as indium tin oxide (ITO) or zinc oxide (ZnO), amorphous MnO_x offers distinctive advantages including multiple accessible oxidation states (Mn^{2+}, Mn^{3+}, Mn^{4+}), natural abundance, and significantly lower cost. Furthermore, the oxygen content in amorphous MnO_x provides an additional parameter for tuning optical and electrical properties, unlike many other amorphous oxides where composition is more constrained. These characteristics make amorphous MnO_x particularly attractive for large-area, cost-sensitive optoelectronic applications while maintaining the beneficial uniformity and processing flexi-

bility common to amorphous materials.

The amorphous structure of materials offers unique advantages over their crystalline counterparts, including better uniformity and greater flexibility in processing [17]. In the case of MnO_x, the amorphous state could lead to interesting photoelectric properties, opening up new prospects for a variety of technological applications, such as two-dimensional (2D) transistors [9], solar cells [11], supercapacitors [18], lithium-ion batteries [19], and optoelectronic devices [20].

Physical vapor deposition (PVD) is a widely used technique for synthesizing thin films of metal oxides [21, 22]. A crucial parameter in this process is the oxygen content, which can significantly influence the stoichiometry, electronic structure and, consequently, the optoelectronic properties of the resulting material. However, the specific impact of oxygen content on the photoelectric properties of amorphous MnO_x thin films has not been systematically investigated to date.

Our study aims to address this gap in the scientific literature. We present a detailed analysis of amorphous MnO_x thin films, focusing on their optical properties, electrical characteristics, and photocurrent measurements. Ultraviolet-visible (UV-Vis) spectroscopy was used to determine optical band gaps, while current-voltage (I-V) characteristics were analyzed to assess electrical conductivity. Photocurrent measurements evaluated the photoelectric response, and numerical simulations modeled the behavior of the most promising sample. A weighted comparative evaluation synthesized the performance across different oxygen levels. This comprehensive approach aims to provide valuable information on the potential of MnO_x thin films for optoelectronic applications.

This research contributes to the fundamental understanding of amorphous MnO_x thin films and paves the way for optimizing these materials for potential applications in optoelectronics. The absence of literature directly related to our results underscores the innovative nature of this study and its potential importance for the future development of devices based on amorphous MnO_x. We will refer to our samples as MnO, omitting the x for simplicity.

2. Experimental Methods

2.1. Thin Film Deposition

The MnO films were deposited using DC magnetron sputtering in an Alliance Concept AC 450 deposition chamber. This 70-liter chamber was pumped using a turbomolecular pump coupled with a mechanical pump, achieving an ultimate pressure of approximately 1×10^{-4} Pa. The Mn target, with a purity of 99.9% and a diameter of 2 inches, was positioned 60 mm from the center of the sample holder.

The substrate holder rotated at 10 rpm with an oscillation range of $\pm 15^{\circ}$ to ensure thickness homogeneity. Target pre-sputtering was performed for 15-20 minutes until voltage stabilization (initial target voltage of approximately 466 V before O_2 introduction), followed by at least 15 minutes of additional cleaning in pure argon atmosphere.Sputtering was performed in an Ar-O_2 atmosphere with a constant current of 100 mA. To maintain a constant total pressure of 0.97 Pa, the argon flow rate was systematically decreased as the oxygen flow rate increased prior to each deposition. No change in gas flow was made during film growth, and the chamber pressure remained highly stable within ± 0.02 Pa. The deposition rates, calculated from the final thickness and deposition time, varied between 3.52 and 3.60 nm/min across the samples. The sputtering system is equipped with mass flow controllers for Ar and O_2, which can be operated either manually or via LabVIEW, allowing precise and reproducible control of the gas flow ratio and ensuring excellent plasma stability throughout the process. Depositions were conducted at room temperature. The specific deposition parameters for each sample, including oxygen flow rates, argon flow rates, calculated oxygen partial pressures, deposition times, and resulting thicknesses are summarized in Table 1. Two types of substrates were used: N-doped silicon (100) wafers (1.5 cm^2) and silica substrates (2.5 cm^2). The substrates were cleaned ex-situ with ethanol and dried at room temperature before each deposition.

This relatively large thickness was selected to ensure that the measured properties are representative of the bulk behaviour of MnO_x and to minimise substrate-related optical or electrical effects [23, 24].

2.2. Characterization Techniques

2.2.1. Optical transmission measurements

The optical properties of the thin films were evaluated using a Perkin Elmer Lambda 950 spectrophotometer. Transmission measurements were

Table 1: Detailed deposition parameters for MnO_x thin films

Sample	O_2 flow (sccm)	Ar flow (sccm)	Total pressure (Pa)	O_2 partial pressure (Pa)	Deposition time (h:min)	Thickness (nm)	Deposition rate (nm/min)
MnO-1	0.94	3.60	0.97	0.201	2:24	515 ± 15	3.58
MnO-2	1.54	3.50	0.97	0.296	2:32	535 ± 15	3.52
MnO-3	1.94	2.80	0.97	0.397	2:30	530 ± 15	3.53
MnO-4	2.54	2.30	0.97	0.509	2:30	540 ± 15	3.60
MnO-5	2.95	1.68	0.97	0.618	2:30	530 ± 15	3.53

conducted over a wavelength range from 200 to 1500 nm. Before each set of measurements, rigorous calibration was performed with a reference blank to ensure the accuracy of the results. The MnO samples were then placed in the measurement cell to record the transmission spectrum. Data analysis allowed the extraction of the band gap energy through Tauc analysis.

2.2.2. Characterization of electrical and photoelectric performance

The performance evaluation of the samples was carried out using OSSILA equipment, adhering to the optimal conditions recommended by the manufacturer. All I–V and photocurrent measurements were performed on MnO_x thin films deposited on silica substrates using a planar electrode configuration with surface contacts. This geometry ensures lateral current flow within the film plane, avoiding interface-related non-linearities that would occur in vertical MnO/Si heterostructures due to band alignment issues.

Figure 1 shows the planar device structure used for electrical characterization. The MnO film on silica substrate is contacted by two golden electrodes in a co-planar configuration, enabling lateral current flow measurement without interfacial complications from substrate band alignment.

Two types of measurements were conducted:

- I(V) curves in darkness:

  The current-voltage I(V) characteristics were recorded under dark conditions over a bias range from -1 V to +1 V. These measurements allowed the characterization of the intrinsic electrical properties of the MnO layers by eliminating the influence of light.

- Transient photocurrent measurements I(t) under constant bias:

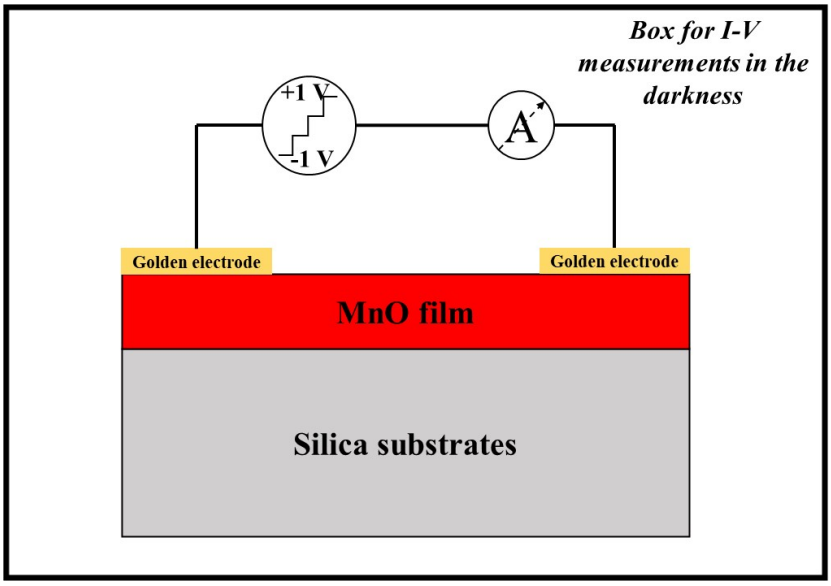

Figure 1: Schematic of the device structure for I-V and photocurrent measurements.

Current-time I(t) measurements were performed under a fixed bias of 0.5 V, following a specific temporal protocol, both in the presence and absence of light. The total measurement duration was 3400 seconds, organized as follows:

- From 0 s to 180 s: the sample was kept in darkness.
- From 180 s to 1700 s: the sample was exposed to illumination under the solar simulator, conforming to the AM1.5G spectrum and an intensity of 100 mW/cm^2.
- From 1700 s to 3400 s: the illumination was turned off.

The solar simulator was positioned at a distance of 8.5 cm from the sample, with an illuminated area of $1.5cm^2$, in accordance with the manufacturer's recommendations. These conditions ensure homogeneous and standardized illumination, allowing precise study of the dynamic response of the devices and the photocurrent generated during the different illumination phases.

2.2.3. Capacitance-Voltage C(V) Measurements

C(V) measurements were performed at 1 MHz in a Metal-Oxide -Semiconductor (MOS) mode using a mercury probe model 802, a Keithley

2400 generator, and a Hewlett Packard 4284 A recorder. The measurements were conducted on MnO layers deposited on N-doped silicon (resistivity of 1 to 10 Ω.cm). Analysis of the curves allowed the extraction of the oxide capacitance (C_{ox}) in the accumulation regime, providing an estimation of the dielectric properties of the thin film.

2.2.4. Thickness measurement

The thickness of the MnO films was measured using a Bruker Dektak DXT profilometer, based on a mechanical stylus scanning technique. The height difference between an uncovered reference area and the film surface was used to assess film thickness with an accuracy of ±5 nm.

2.2.5. X-ray Diffraction Characterization

The structural characterization of the films was performed by XRD using a Bruker D8 Focus diffractometer (Bruker AXS, Karlsruhe, Germany) configured in Bragg-Brentano geometry. The system was equipped with a cobalt X-ray tube (Co Kα radiation, $\lambda = 0.178897$ nm) and a LynxEye linear detector. Diffractograms were collected in air over a 2θ angular range of 20° to 80° with a scanning speed of 0.1° per second and a step size of 0.02°. The operating voltage and current were set to 40 kV and 40 mA, respectively. This configuration allowed for the detection of potential crystalline phases and the confirmation of amorphous structure through the characteristic broad halo pattern.

3. Resultats and Discussion

3.1. Structural analysis

The structure of the films was studied by XRD. Figure 2 shows the complete XRD profile for a MnO-1 sample, which exhibits the characteristic broad halo between 20° and 80° (2θ) without any sharp diffraction peaks. This pattern confirms the amorphous nature of MnO-1 film. Identical XRD patterns were observed for all samples (MnO-2 to MnO-5), indicating that the amorphous structure was maintained across the entire range of oxygen flow rates (0.94 to 2.95 sccm).

The preservation of amorphous structure across different oxygen contents is consistent with our low-temperature deposition process. It is well established that manganese oxide (MnO_x) thin films deposited at room temperature typically maintain their amorphous state, as the transition to crystalline phases (such as Mn_2O_3 or Mn_3O_4) requires high-temperature thermal

annealing, typically above 450 °C [25, 26]. Since our samples underwent no post-deposition annealing, their amorphous nature was preserved regardless of oxygen content.
While the broad halo confirms the absence of long-range crystallographic order, the possibility of short-range ordering at the nanoscale level cannot be excluded. Similar amorphous manganese oxide films have been reported to exhibit local structural variations in Mn-O coordination environments[27] ,which may influence the optoelectronic properties observed in this study.

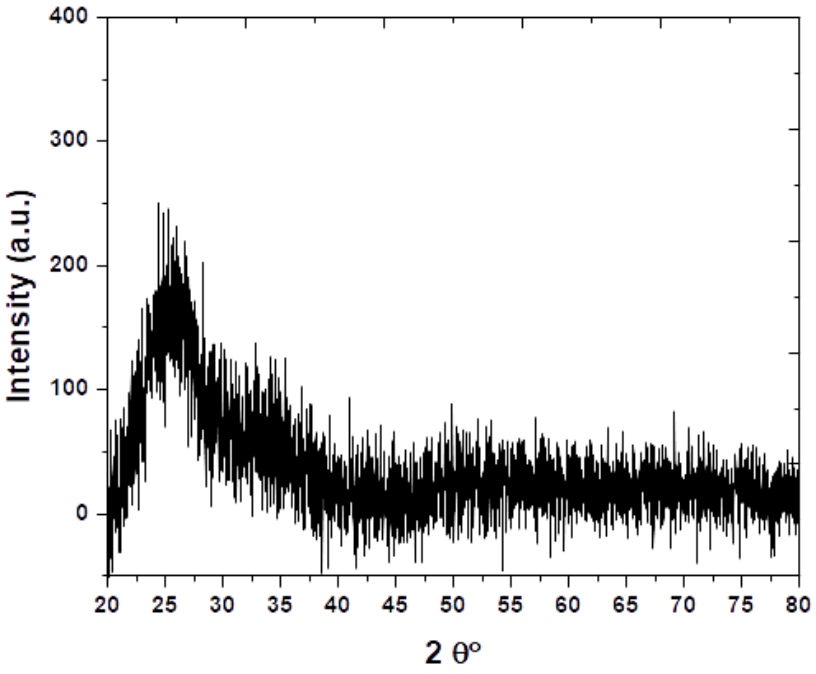

Figure 2: Complete XRD pattern of a representative amorphous MnO-1 film. All samples (MnO-2 to MnO-5) exhibited identical amorphous patterns.

3.2. Optical properties

The optical transmission spectra of amorphous thin films MnO-1 to MnO-5 are shown in Figure 3. Similar behavior is observed for all samples in the UV-vis region (200-800 nm), with almost zero transmission, indicating strong absorption in this spectral range. Above 800 nm, the transmission increases significantly, but with notable variations between samples, highlighting the influence of oxygen content on optical properties in the near-infrared (NIR).

Transmission oscillations are also observed between 1000 nm and 1400 nm, suggesting interference effects related to film thickness or optical resonance phenomena. These oscillations are more or less pronounced, depending on the oxygen content. The main observations regarding variations in transmission as a function of oxygen content are as follows. MnO-1 shows the lowest transmission in the NIR region, indicating higher absorption. This can be attributed to a higher density of defects, such as unsatisfied bonds, resulting from the lack of oxygen to saturate the bonds during deposition. MnO-2 and MnO-3 show intermediate behavior, with higher transmission than MnO-1, suggesting reduced defects due to incorporating a moderate amount of oxygen. MnO-4 shows the highest transmission over a wide range of wavelengths in the NIR, indicating effective defect passivation by oxygen. This suggests that oxygen improves transparency by reducing defects and absorption centers[28, 29]. MnO-5 shows lower transmission than MnO-4 at all wavelengths, despite a higher oxygen content. This indicates that excess oxygen can introduce new types of defects or structural changes that negatively influence transmission. Increasing oxygen levels beyond a certain threshold could alter the structure of the layer, reducing transparency [30].

The optical energy gap (E_g) was determined from the absorption spectra using the Tauc method (Figure 2), based on the relationship:

$$(\alpha h\nu)^n = A(h\nu - E_g)$$

where α is the absorption coefficient, $h\nu$ is the photon energy, A is a constant While amorphous materials can exhibit both direct and indirect transitions, the choice of $n = 2$ for direct allowed transitions is well-established for amorphous manganese oxides and similar transition metal oxides [3, 20, 31]. The absorption edge and yields band gap values consistent with reported literature for amorphous MnO_x systems. The dominance of direct transitions in these materials may be attributed to their short-range order and the specific nature of Mn–O coordination in amorphous networks. The extrapolation of the linear part of the curve $(\alpha h\nu)^2$ as a function of $h\nu$ allows the estimation of Eg. Figure 4 shows the values obtained for the optical energy gap. . The observed variation of E_g with oxygen content can be attributed to modifications in the defect structure and local stoichiometry within the amorphous MnO_x network. At low oxygen flow rates (MnO-1), a higher density of oxygen vacancies introduces donor-like localized states near the conduction band, effectively reducing the optical gap. As oxygen content in-

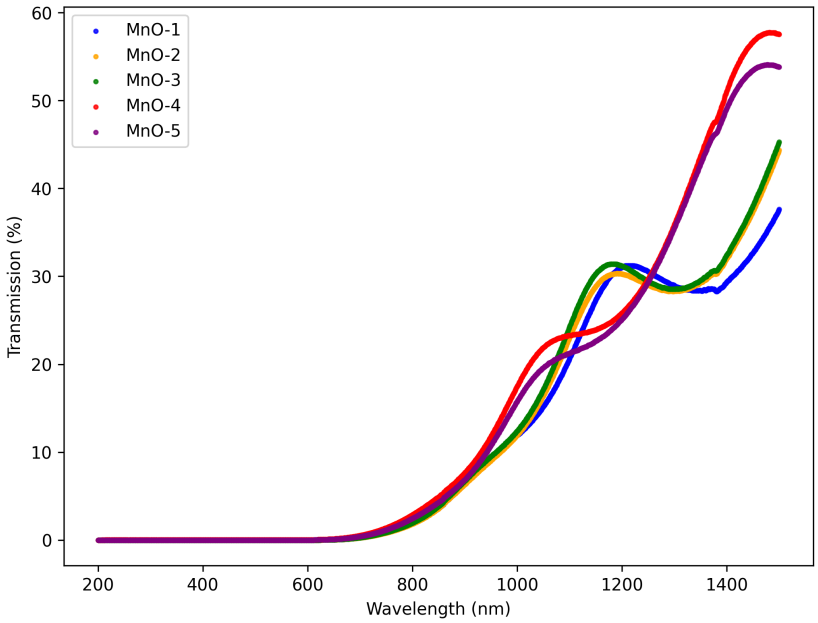

Figure 3: Transmission spectra of MnO samples

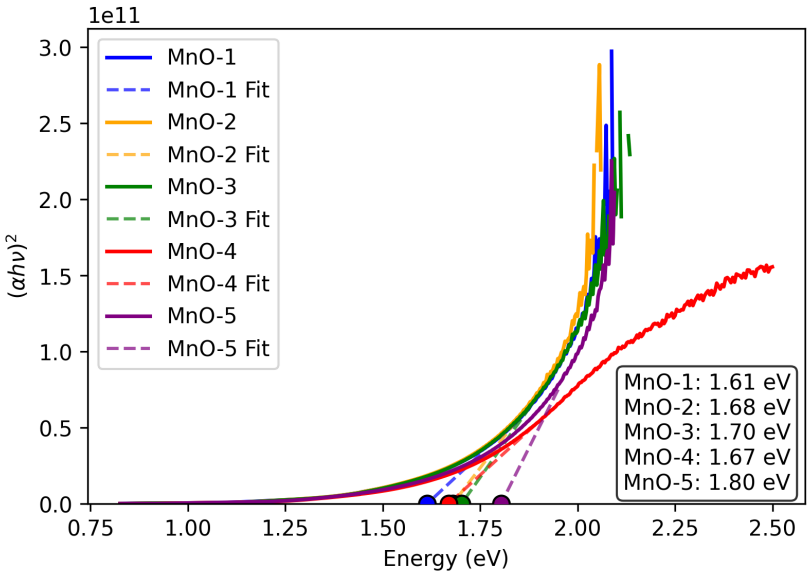

Figure 4: Tauc plot with bandgap estimation of MnO samples

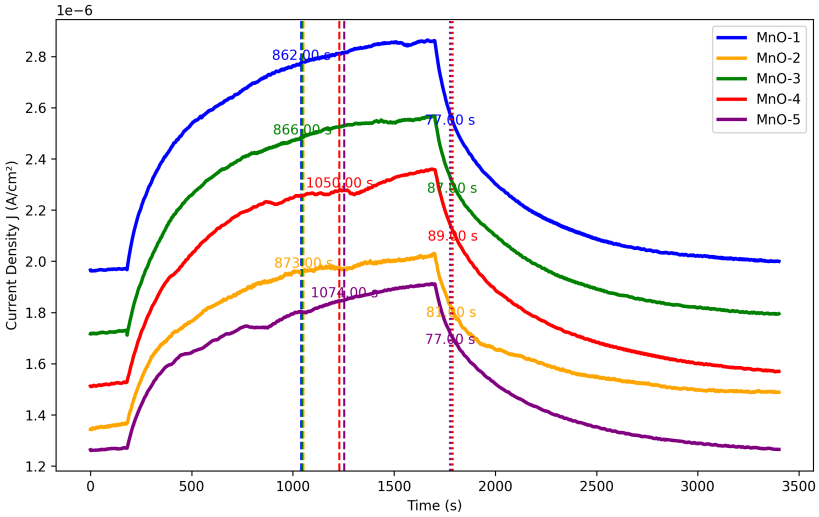

Figure 5: Photocurrent as a function of time of MnO samples

creases (MnO-2 to MnO-4), these defect states are progressively suppressed, leading to a more stoichiometric oxide and consequent widening of the optical band gap. However, for the highest oxygen content (MnO-5), the band gap increases significantly, which may indicate structural modifications or the formation of different defect types that alter the electronic structure. This defect-mediated band gap modulation is consistent with behavior reported in other transition-metal oxide systems, where oxygen vacancies act as intrinsic dopants that modify both carrier concentration and optical absorption characteristics [32, 33, 34].The non-monotonic evolution of E_g across our sample series underscores the complex interplay between oxygen incorporation, defect formation, and electronic structure in amorphous manganese oxide films.

3.3. Photoelectric properties

The current density (J) curves of samples MnO-1 to MnO-5 were recorded under three conditions: in the dark (0–180 s), under illumination (180–1700 s), and after the light was turned off (1700–3400 s). The absolute and normalized current densities are analyzed to understand the samples' photoelectric performance, as shown in the respective figures 5, 6.

To analyze photocurrent dynamics more precisely, we defined rise and fall thresholds adapted to the kinetics observed. The rise time corresponds to

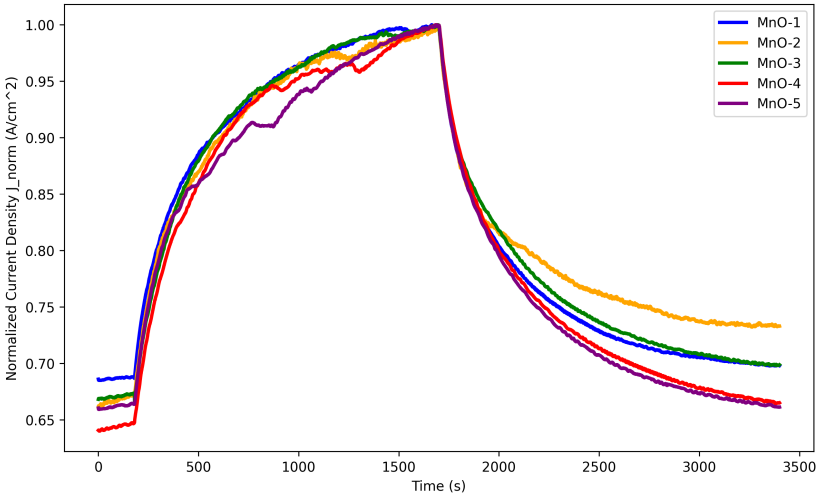

Figure 6: Normalized photocurrent of MnO samples

the current when it reaches 90% of its maximum value, while the fall time is set at 90% of the initial current after 1700 s. This choice enables us to assess both the initial response's speed and the oxide layers' relaxation dynamics. In the dark, all samples show low and stable current densities. The values vary slightly between the samples, ranging from 1.3 μA/cm^2 for MnO-5 to 1.9 μA/cm^2 for MnO-1. These dark currents are attributed to thermally excited charge carriers[35]. The variations between the samples may be due to differences in intrinsic conductivity or defect density in the materials [36]. When the light is turned on at 180 s, a rapid increase in the photocurrent is observed for all samples, reaching a maximum before stabilizing or decreasing slightly. The maximum recorded densities are approximately 2.8 μA/cm^2 for MnO-1, 2.0 μA/cm^2 for MnO-2, 2.5 μA/cm^2 for MnO-3, 2.3 μA/cm^2 for MnO-4, and 1.9 μA/cm^2 for MnO-5. The maximum photocurrent is reached more quickly for some samples (for example, MnO-1 at 862 s and MnO-3 at 866 s). Sample MnO-1 shows the best overall performance, while sample MnO-5 exhibits the weakest response. This rapid increase in photocurrent is due to the generation of electron-hole pairs by light absorption, followed by their effective separation and transport to the electrodes. The differences in maximum performance can be attributed to light absorption efficiency and the quality of the amorphous layer, which is itself influenced by the oxygen content (modifying the defect density and recombination) [37], as illustrated

by the variations in absolute current densities presented in figure 5.
Furthermore, the increase in oxygen content may enhance electron-phonon interactions due to structural modifications and the introduction of localized defect states, which can influence carrier mobility and recombination dynamics under illumination [17, 38]. After the light is turned off at 1700 s, all samples show a rapid drop in current density, followed by a gradual relaxation towards their initial dark levels. The characteristic decay times are approximately 77.60 s for MnO-1, 81.60 s for MnO-2, 87.40 s for MnO-3, 89.30 s for MnO-4, and 77.0 s for MnO-5. The rapid decrease reflects the immediate cessation of charge carrier generation by illumination, while the slow relaxation is influenced by processes such as recombination of residual carriers or trapping/de-trapping in defects or at interfaces. In our case, the decay is relatively slow, probably because of prolonged recombination processes and the possible presence of electron traps that influence the relaxation of the charge carrier [38, 39]. A lower threshold, such as 10%, would be irrelevant, as it would only be reached after a very long time, making the analysis difficult and more sensitive to signal fluctuations. Using the 90% threshold, therefore, allows us to focus on the rapid initial decay phase, as seen in the normalized current density figure.
Although MnO-1 contains a higher overall defect density relative to oxygen-rich samples, the shorter photoresponse decay time suggests dominance of shallow recombination centers, leading to faster carrier recombination. Conversely, in oxygen-rich MnO-5, deeper oxygen-related traps contribute to prolonged decay times, consistent with decreased mobility and increased structural disorder[38, 17]. The MnO-5 sample, despite the highest oxygen content, shows a decay time equivalent to that of MnO-1 (77 s). This observation suggests that for MnO-5, other mechanisms (e.g. enhanced conduction via secondary phase formation or structural reorganization) could compensate for the effect of traps and accelerate carrier recombination.
The absence of a monotonic trend in electrical resistance and maximum current density with oxygen content reflects the competing roles of oxygen in amorphous MnO_x films: while moderate oxygen incorporation passivates defects and enhances carrier lifetime, excessive oxygen introduces structural disorder and reduces charge carrier density. This trade-off results in optimal performance at intermediate oxygen flow rates (MnO-1), consistent with observations in other transition metal oxide systems[40].
The normalized curves J_{norm} for all samples show similar behaviors when normalized, with comparable kinetics under illumination and during relaxation.

This suggests that the fundamental mechanisms, such as carrier generation and transport as well as their recombination, are similar between the samples. The differences observed in the overall performance are therefore mainly due to the only parameter common to these samples, namely the oxygen content.

The results highlight that the photoelectric performance varies between samples MnO-1 to MnO-5. The observed differences, both in terms of dark current, maximum photocurrent, and decay times, suggest a significant influence of oxygen content on the properties of the amorphous layers studied.

3.4. I-V electrical analyses

Figure 7 shows the I(V) current-voltage curves for the five MnO samples. The measurements were each performed twice consecutively under identical conditions (bias range and ambient temperature) to verify repeatability. The two measurement sets produced identical overlapping curves, confirming the reproducibility and stability of the data.I(V) curves allow direct assessment of the electrical conductivity of each sample under DC bias. The linear and symmetrical shape of the curves around the origin suggests ohmic behavior, indicating the absence of significant potential barriers at the contacts. However, the slope of each curve, inversely proportional to electrical resistance, varies from sample to sample as a function of oxygen content.

- MnO-1 ($R = 2.53 \times 10^5 \Omega$): It Presents the steepest slope, which reflects lower resistance. The moderate oxygen content limits the formation of defects in the crystal lattice, favoring charge carrier transport.

- MnO-2 ($R = 3.68 \times 10^5 \Omega$) and MnO-3 ($R = 3.00 \times 10^5 \Omega$): Display intermediate resistances, reflecting a compromise between conduction and defect formation. This result is consistent with photocurrent measurements, where MnO-2 and MnO-3 also showed a balance between carrier generation and recombination.

- MnO-4 ($R = 3.36 \times 10^5 \Omega$): Approaches the resistance range of MnO-3, but a higher oxygen content can induce more diffusion or recombination centers, slightly reducing conductivity compared to MnO-2 and MnO-3.

- MnO-5 ($R = 4.10 \times 10^5 \Omega$): Has the highest resistance of the set, suggesting that excess oxygen introduces additional defects into the material, further impeding current flow.

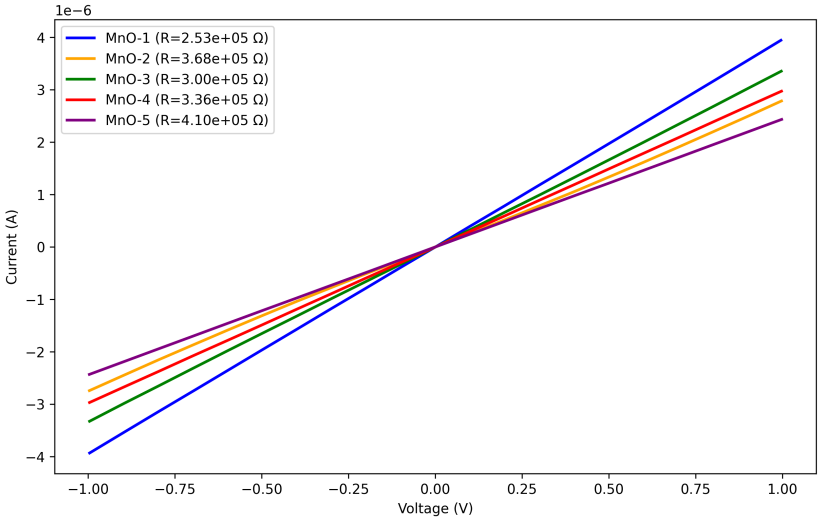

Figure 7: I(V) current-voltage curves for the MnO samples

Comparing these results with those obtained in the photocurrent regime, we observe that oxygen, while influencing carrier generation under illumination, also acts on electrical conductivity when not under illumination. Lightly doped samples (MnO-1) favor charge transport, while highly doped samples (MnO-5) suffer from increased resistance that can impair optoelectronic performance. The MnO-2 and MnO-3 samples exhibit a balanced character in terms of ohmic conduction.

3.5. Weighted Comparative Evaluation for Photovoltaic Applications

To objectively compare the overall optoelectronic performance of the MnO thin films (MnO-1 to MnO-5) with the increasing oxygen content for photovoltaic applications, we performed a weighted comparative evaluation using a set of weights tailored to the requirements of solar cells. The weighting coefficients (30% for current density and resistance, 20% for band gap, 10% for rise and decay times) were defined based on the relative influence of each parameter on device performance according to established photovoltaic evaluation criteria[41, 42, 43].In photovoltaic devices, the key performance aspects are as follows:

- **Maximum Current Density (J_{max}) (30%):** A high current density is crucial for maximizing the short-circuit current and overall power conversion efficiency. Thus, this parameter is given a high weight.

- **Electrical Resistance (R) (30%):** Low resistance minimizes ohmic losses and improves the fill factor, which is critical for device performance.
- **Optical Band Gap (Gap) (20%):** The band gap determines the spectral range of light absorption. An optimal gap (typically in the range of 1.3–1.7 eV for efficient solar conversion) ensures effective utilization of the solar spectrum.
- **Rise Time (10%) and Decay Time (10%):** In photovoltaic applications the dynamic response is less critical since solar irradiation changes slowly. Therefore, these parameters are assigned lower weights.

Table 2: Experimental data for the MnO thin films.

Sample	Rise Time (s)	Decay Time (s)	J_{max} (A/cm^2)	Band Gap (eV)	Resistance (Ω)
MnO-1	862	77	2.86×10^{-6}	1.61	2.53×10^5
MnO-2	873	81	2.03×10^{-6}	1.68	3.00×10^5
MnO-3	866	87	2.57×10^{-6}	1.70	3.36×10^5
MnO-4	1054	89	2.36×10^{-6}	1.67	3.68×10^5
MnO-5	1074	77	1.91×10^{-6}	1.80	4.10×10^5

For each parameter, a normalized score S_i on a scale of 1 to 10 is assigned according to linear normalization. For a parameter where a higher value is preferable (maximum current density), the formula used is:

$$S_i = 1 + \frac{9\,(X - X_{\min})}{X_{\max} - X_{\min}}$$

and for a parameter where a lower value is preferable (rise time, decay time, band gap, and electrical resistance), normalization is performed in the reverse manner:

$$S_i = 10 - \frac{9\,(X - X_{\min})}{X_{\max} - X_{\min}}$$

where X represents the experimental value of the parameter, and $X_{\min}$ and $X_{\max}$ the observed minimum and maximum values (details are given in the figures and summarized in Table 2). The final score for each sample is then calculated by:

$$S_{\text{final}} = 0.10\,S_{\text{rise}} + 0.10\,S_{\text{decay}} + 0.30\,S_{J_{max}} + 0.20\,S_{\text{gap}} + 0.30\,S_R.$$

Table 3: Weighted comparative evaluation of the optoelectronic performance of the MnO thin films for photovoltaic applications.

Sample	Rise Time (score)	Decay Time (score)	J_{max} (score)	Band Gap (score)	Resistance (score)	Total Score
MnO-1	10.00	10.00	10.00	10.00	10.00	10.00
MnO-2	9.53	7.00	2.14	6.68	7.31	5.82
MnO-3	9.83	2.50	7.25	5.74	5.25	6.12
MnO-4	2.01	1.00	5.26	7.16	3.41	4.33
MnO-5	1.00	10.00	1.00	1.00	1.00	1.90

Table 3 summarizes the scores attributed to each sample based on these weighted photovoltaic-oriented criteria. The results indicate that the MnO-1 sample offers the best overall performance for photovoltaic applications, primarily due to its superior current density and low resistance. This analysis underscores the importance of adapting the weighting scheme to the specific requirements of the target application.

3.6. Numerical Simulation of the MnO-1 Sample

Given its superior performance, the MnO-1 sample was selected for an in-depth analysis using numerical simulations. These simulations aim to model the behavior of the photocurrent under illumination and enhance the experimental results.

3.6.1. Polynomial Fitting of the Photocurrent

The first step of the analysis involved fitting the experimental photocurrent curve I(t) with a polynomial function. This approach is based on the principle that polynomial functions can provide a reasonable approximation of complex curve shapes, allowing for the smoothing of noisy experimental data and obtaining an analytical representation useful for subsequent modeling steps. This polynomial fitting was performed using the `curve_fit` function from the `scipy.optimize` library in Python [44]. To evaluate the robustness of the polynomial fit, the entire set of experimental data was divided into a training set and a test set using the `train_test_split` function from the `sklearn.model_selection` library, with 20% of the data allocated to the test set. This procedure validates the polynomial model's ability to generalize to data not used for fitting.

A third-order polynomial fit was identified as optimally describing the shape of the experimental photocurrent curve (see Figure 8 for a visual representation of the fit). The coefficients of this third-order polynomial, obtained by

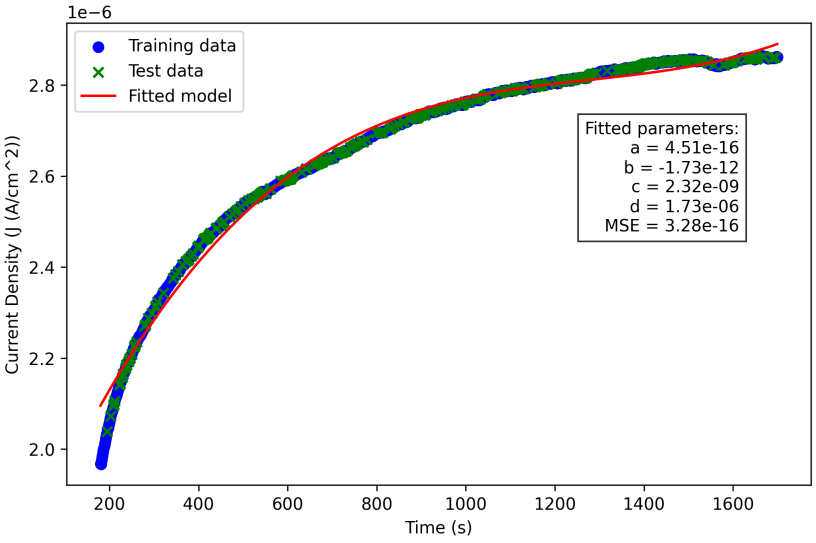

Figure 8: Polynomial Fitting of the MnO-1 Photocurrent

fitting to the training set, have the following values: $a = 4.42 \times 10^{-16}, b = -1.70 \times 10^{-12}, c = 2.29 \times 10^{-9} and\ d = 1.74 \times 10^{-6}$. These coefficients quantify the nonlinear relationship between the applied voltage and the photocurrent in the MnO-1 material. The quality of the fit was evaluated by calculating the mean squared error (MSE) in the test set, which is extremely low at 3.28×10^{-16}. Such a low MSE indicates an excellent fit of the polynomial model to the experimental data, validating the relevance of this analytical approximation [3]. Figure8 shows a direct overlay of experimental and simulated photocurrent data, confirming their near-perfect agreement, while the very low MSE value quantitatively validates the residual analysis of the model fit.

3.6.2. Equivalent Circuit Modeling

To model the dynamic electrical behavior of MnO-1 under illumination, an equivalent electrical circuit consisting of a series resistance R_s, a shunt resistance R_{sh}, and a capacitance C was considered (see figure9). This model was chosen for the following reasons:

- Series Resistance R_s: models the ohmic losses within the system, including the resistance of electrical contacts, interconnections, and the intrinsic resistance of the thin film. In this study, the value of the series

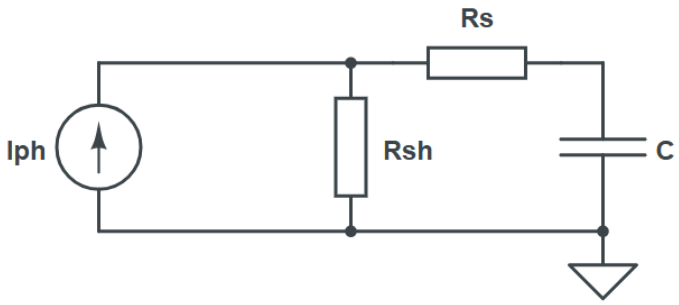

Figure 9: Equivalent electrical circuit of MnO-1

resistance was experimentally determined from the slope of the linear region at a high field of the current-voltage I(V) curve of the sample measured in the dark. This approach, based on the analysis of conductance at a high field, ensures that the value of R_s used in the model accurately reflects the ohmic transport characteristics of the material. Specifically, R_s accounts for the overall resistance to conduction, which is particularly relevant in the case of an amorphous material, where the mobility of charge carriers may be limited.

- Shunt Resistance R_{sh}: accounts for potential leakage currents due to defects, thickness irregularities, or micro-damage within the thin film, as well as other non-ideal conduction paths. R_{sh} helps distinguish the useful photocurrent from parasitic current components.

- Capacitance C: represents the ability of the metal oxide layer to accumulate charges, an intrinsic dielectric behavior of the material. In addition, in the context of an amorphous thin film, C models the effects related to the interface and the distribution of trapped states, including charge accumulation and relaxation phenomena.

To determine the values of the R_{sh} and C parameters of the equivalent circuit model, a fitting approach based on the `scipy.optimize` library in Python was used. In this approach, the series resistance R_s was fixed at a value of $3.33 \times 10^5 \Omega$, determined independently from the measurements of I(V). The circuit model, implemented as a differential equation, was fitted to the experimental photocurrent data filtered over the time interval of 180 to 1700

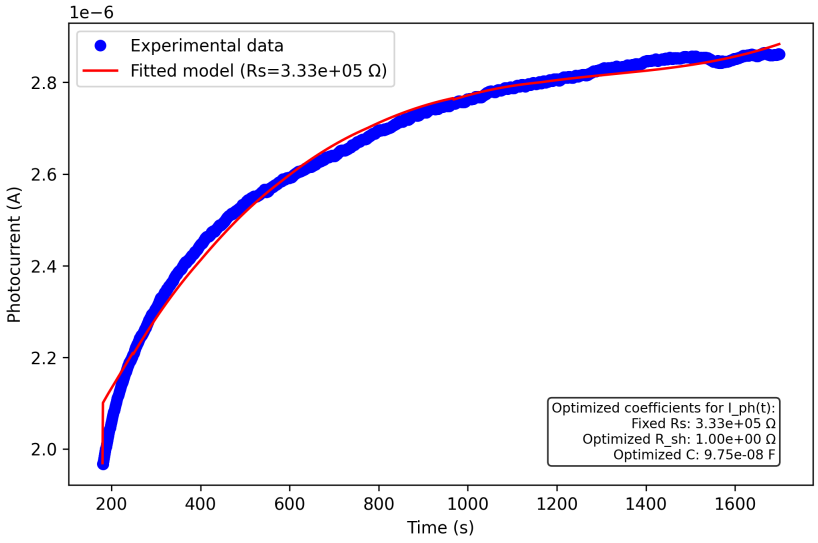

Figure 10: Model fit with fixed R_s to the MnO-1 photocurrent

s (illumination phase). The following differential equation:

$$C\frac{dI(t)}{dt} + I(t)(\frac{1}{R_{sh}} - \frac{1}{R_s}) = I_{ph}(t), \qquad I(0) = 1.9692e^{-06}A.$$

was solved numerically using the `odeint` function from the `scipy.integrate` library. The Python tool determined the values of the parameters R_{sh} and C minimize the mean squared error (MSE) between the polynomial photocurrent curve and the simulated circuit response. The equivalent circuit model fitting yielded similarly excellent agreement with the experimental data, further validating the polynomial approximation approach.
The optimized values of the equivalent circuit parameters, obtained by setting the series resistance to $R_s = 3.33 \times 10^5\ \Omega$ (determined from the experimental I–V curve), are: $R_{sh} = 1.00\ \Omega$ and $C = 9.75 \times 10^{-8}\ F$. The low value of R_{sh} suggests the presence of significant leakage paths or significant parallel conduction within the sample, which could be related to the amorphous nature of the oxide layer and the presence of defects.

To further validate the hypothesis of the presence of a capacitor, and to confirm the value extracted by simulation, capacitance-voltage (C−V) measurements were carried out at a frequency of 1 MHz in the Metal-Oxide-Semiconductor (MOS) configuration. The C−V curve obtained (see figure11),

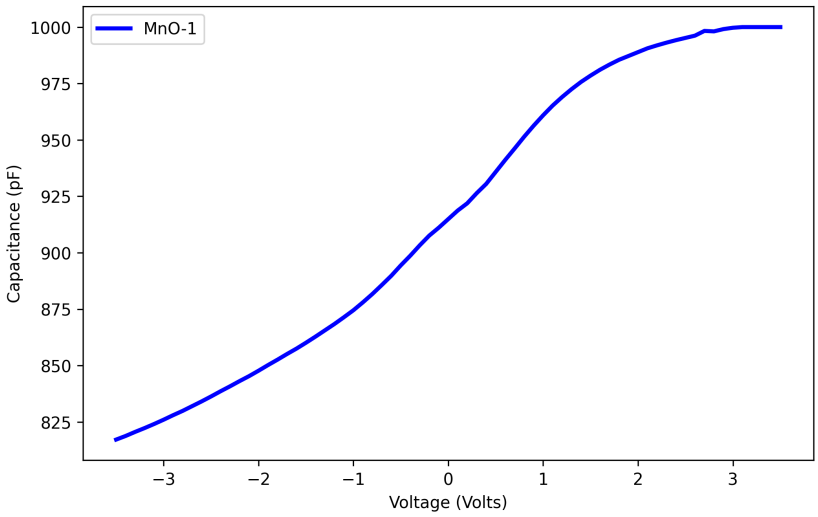

Figure 11: capacitance-voltage C−V measurements of MnO-1 sample

measured at this frequency, shows the typical shape of a capacitor in the accumulation regime, with a capacitance that increases with positive bias voltage. The maximum capacitance reached in the accumulation regime is approximately around 1000 pF (1 nF), which corresponds to $10^{-9}F$. This value is about two orders of magnitude smaller than the capacitance value $C = 9.75 \times 10^{-8}F$ extracted from the equivalent circuit model and photocurrent simulations. Despite this significant difference, the qualitative and semi-quantitative agreement between the independent C–V measurements and the modeling results reinforces the relevance of the chosen circuit model and the validity of the extracted parameters.

In summary, this study analyzed the MnO-1 photocurrent by combining experimental measurements, equivalent electrical circuit modeling, Python numerical simulations and independent C−V measurements. The polynomial fit of the photocurrent, performed using Python's curve_fit function and validated by a train-test split approach, with an extremely low mean-square error MSE), determined the circuit parameters R_s, R_{sh}, C) via a fitting procedure based on curve_fit. curve_fit and solving a differential equation with odeint, setting R_s to an experimental value, and setting R_s to an experimental value, and cross-validation with C−V measurements have enabled us to characterize the electrical and photoelectric properties of this material. The results suggest a behavior influenced by the amorphous na-

ture of the metal oxide, with significant significant series resistance, potential leakage paths, and capacitive behavior consistent with a dielectric material exhibiting trapped states.

4. Conclusion

In this study, we explored the optical and electrical properties of amorphous MnO thin films as a function of oxygen content. The results highlight the significant influence of oxygen on the optoelectronic performance of these materials.

Optical transmission spectra revealed strong absorption in the UV-visible region for all samples, with notable variations in the near-infrared (NIR) depending on oxygen content. An optimal oxygen content (MnO-4) improved transparency by reducing defects, whereas excess oxygen (MnO-5) introduced new defects, reducing transmission. These observations underscore the importance of precisely controlling oxygen content to optimize the optical properties of thin films.

The analysis of photoelectric properties showed that photocurrent dynamics are also influenced by oxygen content. A moderate content promotes carrier generation, but excess oxygen can introduce electron traps, delaying recombination. I-V curves revealed ohmic behavior, with variable resistances depending on oxygen content, where lower content favored higher conductivity.

For photovoltaic applications, the MnO-1 sample demonstrated the best overall performance, due to high current density and low resistance. Optimizing oxygen doping thus appears crucial for tailoring the photoconductive response of films to meet optoelectronic application requirements.

Finally, numerical simulations and equivalent circuit modeling precisely characterized the electrical properties of MnO-1, validating the presence of leakage paths and capacitive behavior. These results suggest that fine adjustments in composition can lead to significant improvements for advanced photovoltaic applications.

The demonstrated tunability of optoelectronic properties through oxygen content control makes these amorphous MnO_x films promising for integration into devices such as thin-film photodetectors and as hole transport layers in solar cells. Future work will focus on fabricating heterojunction devices and evaluating their performance and stability under operational conditions.

References

[1] S. Sahoo, K. Y. Wickramathilaka, E. Njeri, D. Silva, S. L. Suib, A review on transition metal oxides in catalysis, Frontiers in Chemistry 12 (2024). URL: https://www.frontiersin.org/journals/chemistry/articles/10.3389/fchem.2024.1374878/full. doi:10.3389/fchem.2024.1374878, publisher: Frontiers.

[2] M. Nurul Islam, Fabrication and Characterization of Manganese Based Thin Films in Optoelectronic Applications, Asian Journal of Electrical Sciences 12 (2023) 14–16. URL: https://ajesjournal.org/index.php/ajes/article/view/3665. doi:10.51983/ajes-2023.12.1.3665.

[3] M. Makhlouf, Preparation and optical characterization of β-MnO2 nano thin films for application in heterojunction photodiodes, Sensors and Actuators A: Physical 279 (2018) 145–156. URL: https://linkinghub.elsevier.com/retrieve/pii/S0924424717320277. doi:10.1016/j.sna.2018.06.003.

[4] A. Gasparotto, C. Maccato, A. Petala, S. Bebelis, C. Sada, D. I. Kondarides, D. Barreca, Nanoscale Mn3O4 Thin Film Photoelectrodes Fabricated by a Vapor-Phase Route, ACS Applied Energy Materials 2 (2019) 8294–8302. URL: https://doi.org/10.1021/acsaem.9b01773. doi:10.1021/acsaem.9b01773, publisher: American Chemical Society.

[5] C.-C. Lin, P.-Y. Lin, Capacitance Measurements of MnOX Films Deposited by Reactive Sputtering of a Mn Target, Electrochemistry 79 (2011) 458–463. doi:10.5796/electrochemistry.79.458.

[6] M. A. Dahamni, M. Ghamnia, S. E. Naceri, C. Fauquet, D. Tonneau, J.-J. Pireaux, A. Bouadi, Spray Pyrolysis Synthesis of Pure and Mg-Doped Manganese Oxide Thin Films, Coatings 11 (2021) 598. URL: https://www.mdpi.com/2079-6412/11/5/598. doi:10.3390/coatings11050598, number: 5 Publisher: Multidisciplinary Digital Publishing Institute.

[7] F. Zhou, A. Izgorodin, R. K. Hocking, L. Spiccia, D. R. MacFarlane, Electrodeposited MnOx Films from Ionic Liquid for Electrocatalytic

Water Oxidation, Advanced Energy Materials 2 (2012) 1013–1021. URL: https://onlinelibrary.wiley.com. doi:10.1002/aenm.201100783.

[8] H. Jamil, M. Khaleeq-ur Rahman, I. M. Dildar, S. Shaukat, Structural and optical properties of manganese oxide thin films deposited by pulsed laser deposition at different substrate temperatures, Laser Physics 27 (2017) 096101. URL: https://dx.doi.org/10.1088/1555-6611/aa7cc8. doi:10.1088/1555-6611/aa7cc8, publisher: IOP Publishing.

[9] J. Yuan, C. Jian, Z. Shang, Y. Yao, B. Wang, Y. Li, R. Wang, Z. Fu, M. Li, W. Hong, X. He, Q. Cai, W. Liu, Controllable synthesis of nonlayered high-κ Mn3O4 single-crystal thin films for 2D electronics, Nature Communications 16 (2025) 964. URL: https://www.nature.com/articles/s41467-025-56386-9. doi:10.1038/s41467-025-56386-9.

[10] S. Isber, E. Majdalani, M. Tabbal, T. Christidis, K. Zahraman, B. Nsouli, Study of manganese oxide thin films grown by pulsed laser deposition, Thin Solid Films 517 (2009) 1592–1595. URL: https://linkinghub.elsevier.com/retrieve/pii/S0040609008011504. doi:10.1016/j.tsf.2008.09.097.

[11] D. R. Inchara, S. C. Gurumurthy, M. S. Murari, M. D. Daivajna, Structural, optical and electrical studies of non-toxic oxide- RMnO3 [R=Y, Er, Yb] hexagonal manganite thin-films, Thin Solid Films 795 (2024) 140321. URL: https://linkinghub.elsevier.com/retrieve/pii/S0040609024001238. doi:10.1016/j.tsf.2024.140321.

[12] P. Fau, J. Bonino, J. Demai, A. Rousset, Thin films of nickel manganese oxide for NTC thermistor applications, Applied Surface Science 65-66 (1993) 319–324. URL: https://linkinghub.elsevier.com/retrieve/pii/0169433293906796. doi:10.1016/0169-4332(93)90679-6.

[13] M. Chigane, M. Ishikawa, M. Izaki, Preparation of manganese oxide thin films by electrolysis/chemical deposition and electrochromism, Journal of the Electrochemical Society 148 (2001) D96. URL:

https://iopscience.iop.org/article/10.1149/1.1376637/meta, publisher: IOP Publishing.

[14] P. Fau, J. Bonino, A. Rousset, Electrical properties of sputtered MnO2 thin films, Applied Surface Science 78 (1994) 203–210. URL: https://linkinghub.elsevier.com/retrieve/pii/0169433294001111. doi:10.1016/0169-4332(94)00111-1.

[15] H. Xia, W. Xiao, M. Lai, L. Lu, Facile Synthesis of Novel Nanostructured MnO2Thin Films and Their Application in Supercapacitors, Nanoscale Research Letters 4 (2009) 1035. URL: https://link.springer.com/10.1007/s11671-009-9352-4. doi:10.1007/s11671-009-9352-4.

[16] P. Prabukanthan, R. Lakshmi, G. Harichandran, T. Tatarchuk, Photovoltaic device performance of pure, manganese (Mn2+) doped and irradiated CuInSe2 thin films, New Journal of Chemistry 42 (2018) 11642–11652. URL: https://pubs.rsc.org/en/content/articlelanding/2018/nj/c8nj01056k. doi:10.1039/C8NJ01056K, publisher: The Royal Society of Chemistry.

[17] J. E. Medvedeva, D. B. Buchholz, R. P. H. Chang, Recent Advances in Understanding the Structure and Properties of Amorphous Oxide Semiconductors, Advanced Electronic Materials 3 (2017) 1700082. URL: https://onlinelibrary.wiley.com/doi/abs/10.1002/aelm.201700082. doi:10.1002/aelm.201700082.

[18] M. A. Borysiewicz, M. Wzorek, M. Myśliwiec, J. Kaczmarski, M. Ekielski, MnO2 ultrathin films deposited by means of magnetron sputtering: Relationships between process conditions, structural properties and performance in transparent supercapacitors, Superlattices and Microstructures 100 (2016) 1213–1220. URL: https://linkinghub.elsevier.com/retrieve/pii/S074960361631268X. doi:10.1016/j.spmi.2016.11.002.

[19] X.-H. Ma, Q.-Y. Wan, X. Huang, C.-X. Ding, Y. Jin, Y.-B. Guan, C.-H. Chen, Synthesis of three-dimensionally porous MnO thin films for lithium-ion batteries by improved Electrostatic Spray Deposition technique, Electrochimica Acta 121 (2014) 15–20. URL:

https://linkinghub.elsevier.com/retrieve/pii/S0013468613024389. doi:10.1016/j.electacta.2013.12.004.

[20] F. Chahshouri, E. Khani, H. Savaloni, R. Savari, Nano-Structural Characteristics and Optical and Electrical Properties of Obliquely Deposited Manganese Oxide Thin Films, SRPH Journal of Fundamental Sciences and Technology (2021). URL: http://sjfst.srpub.org/article-6-129-en.html. doi:10.47176/sjfst.3.4.1.

[21] W. Hourani, C. Rousselot, K. B. J.-I. N'Djoré, A. Billard, M. Arab Pour Yazdi, Y. Makoudi, Thermal Annealing Effect on the Structure, Optical and Electrical Properties of Lanthanum Manganite Thin Films Prepared by Reactive Co-Sputtering, Electronic Materials 3 (2022) 291–300. URL: https://www.mdpi.com/2673-3978/3/4/25. doi:10.3390/electronicmat3040025.

[22] K. B. J.-I. N'Djoré, M. Grafouté, Y. Makoudi, W. Hourani, C. Rousselot, Tuning the Electrical Properties of Tungsten Oxide Thin Films Deposited by Reactive Magnetron Sputtering, Coatings 12 (2022) 274. URL: https://www.mdpi.com/2079-6412/12/2/274. doi:10.3390/coatings12020274.

[23] A. El-Denglawey, M. M. Makhlouf, M. Dongol, The effect of thickness on the structural and optical properties of nano ge-te-cu films, Results in Physics 10 (2018) 714–720. URL: https://doi.org/10.1016/j.rinp.2018.07.054. doi:10.1016/j.rinp.2018.07.054.

[24] E. S. Shim, H. S. Kang, J. S. Kang, J. H. Kim, S. Y. Lee, Effect of the variation of film thickness on the structural and optical properties of zno thin films deposited on sapphire substrate using pld, Applied Surface Science 186 (2002) 474–476. URL: https://doi.org/10.1016/S0169-4332(01)00746-2. doi:10.1016/S0169-4332(01)00746-2.

[25] G. Balamurugan, M. Jayachandran, C. Sanjeeviraja, Impact of annealing temperature on MnO2 thin films: Morphological, structural, and electrical properties, Journal of Materials Science: Materials in Electronics 28 (2017) 8425–8433. URL:

https://doi.org/10.1007/s10854-017-6487-4. doi:10.1007/s10854-017-6487-4.

[26] S. Lee, D. Kim, J. Park, H. Lee, Thermal crystallization of amorphous manganese oxide thin films prepared by chemical solution deposition, Thin Solid Films 519 (2011) 6746–6750. URL: https://doi.org/10.1016/j.tsf.2011.04.075. doi:10.1016/j.tsf.2011.04.075.

[27] H. Wang, Q. Li, Y. Zhang, L. Chen, J. Zhao, Structural evolution of amorphous manganese oxides with oxygen content: XAS and PDF studies, Journal of Physical Chemistry C 124 (2020) 15668–15677. URL: https://doi.org/10.1021/acs.jpcc.0c03485. doi:10.1021/acs.jpcc.0c03485.

[28] L. M. Wong, S. Y. Chiam, J. Q. Huang, S. J. Wang, J. S. Pan, W. K. Chim, Role of oxygen for highly conducting and transparent gallium-doped zinc oxide electrode deposited at room temperature, Applied Physics Letters 98 (2011) 022106. URL: https://pubs.aip.org/apl/article/98/2/022106/122365/. doi:10.1063/1.3541885.

[29] F. Wu, X. Tong, Z. Zhao, J. Gao, Y. Zhou, P. Kelly, Oxygen-controlled structures and properties of transparent conductive SnO2:F films, Journal of Alloys and Compounds 695 (2017) 765–770. URL: https://www.sciencedirect.com/science/article/pii/S0925838816324926. doi:10.1016/j.jallcom.2016.08.114.

[30] P. Salunkhe, M. A. A V, D. Kekuda, Investigation on tailoring physical properties of Nickel Oxide thin films grown by dc magnetron sputtering, Materials Research Express 7 (2020) 016427. URL: https://iopscience.iop.org/article/10.1088/2053-1591/ab69c5. doi:10.1088/2053-1591/ab69c5.

[31] S. K. J. AL-ANI, Determination of the optical gap of amorphous materials, International Journal of Electronics 75 (1993) 1153–1163. URL: https://doi.org/10.1080/00207219308907191. doi:10.1080/00207219308907191, publisher: Taylor & Francis _eprint: https://doi.org/10.1080/00207219308907191.

[32] J. Robertson, Band gaps and defect states in transition metal oxides, Physical Review B 63 (2001) 245108. URL: https://doi.org/10.1103/PhysRevB.63.245108. doi:10.1103/PhysRevB.63.245108.

[33] X. Chen, Z. Wang, J. Liu, H. Li, Y. Zhao, Oxygen vacancy induced band gap narrowing of zno nanostructures by an electrochemically active biofilm, Applied Surface Science 427 (2018) 604–612. URL: https://doi.org/10.1016/j.apsusc.2017.08.225. doi:10.1016/j.apsusc.2017.08.225.

[34] X. Gao, Y. Zhang, P. Liu, J. Zhao, L. Wang, Role of oxygen vacancies in the optical properties of zno and tio_2 thin films, Journal of Applied Physics 119 (2016) 215304. URL: https://doi.org/10.1063/1.4953181. doi:10.1063/1.4953181.

[35] E. A. Duijnstee, V. M. Le Corre, M. B. Johnston, L. J. A. Koster, J. Lim, H. J. Snaith, Understanding Dark Current-Voltage Characteristics in Metal-Halide Perovskite Single Crystals, Physical Review Applied 15 (2021) 014006. URL: https://link.aps.org/doi/10.1103/PhysRevApplied.15.014006. doi:10.1103/PhysRevApplied.15.014006.

[36] S. Ghosh, G. Sun, T. A. Morgan, G. T. Forcherio, H.-H. Cheng, G.-E. Chang, Dark Current Analysis on GeSn p-i-n Photodetectors, Sensors 23 (2023) 7531. URL: https://www.mdpi.com/1424-8220/23/17/7531. doi:10.3390/s23177531.

[37] A. M. Oni, A. S. Mohsin, M. M. Rahman, M. B. Hossain Bhuian, A comprehensive evaluation of solar cell technologies, associated loss mechanisms, and efficiency enhancement strategies for photovoltaic cells, Energy Reports 11 (2024) 3345–3366. URL: https://linkinghub.elsevier.com/retrieve/pii/S2352484724001525. doi:10.1016/j.egyr.2024.03.007.

[38] J. Strand, M. Kaviani, D. Gao, A.-M. El-Sayed, V. V. Afanas'ev, A. L. Shluger, Intrinsic charge trapping in amorphous oxide films: status and challenges, Journal of Physics: Condensed Matter 30 (2018) 233001. URL: https://dx.doi.org/10.1088/1361-648X/aac005. doi:10.1088/1361-648X/aac005, publisher: IOP Publishing.

[39] D. Wrana, T. Gensch, B. R. Jany, K. Cieślik, C. Rodenbücher, G. Cempura, A. Kruk, F. Krok, Photoluminescence imaging of defects in TiO2: The influence of grain boundaries and doping on charge carrier dynamics, Applied Surface Science 569 (2021) 150909. URL: https://linkinghub.elsevier.com/retrieve/pii/S016943322101967X. doi:10.1016/j.apsusc.2021.150909.

[40] L. Gong, W. Zhang, X. Chen, H. Liu, Oxygen partial pressure dependent non-monotonic conductivity in cuo thin films: The role of oxygen vacancies and structural disorder, Applied Surface Science 578 (2022) 151894. URL: https://doi.org/10.1016/j.apsusc.2021.151894. doi:10.1016/j.apsusc.2021.151894.

[41] M. A. Green, Analytical expressions for the comparative efficiency of photovoltaic cells, Solar Energy Materials and Solar Cells 102 (2012) 1–7. URL: https://doi.org/10.1016/j.solmat.2012.02.019. doi:10.1016/j.solmat.2012.02.019.

[42] W. Shockley, H. J. Queisser, Detailed balance limit of efficiency of p–n junction solar cells, Journal of Applied Physics 32 (1961) 510–519. URL: https://doi.org/10.1063/1.1736034. doi:10.1063/1.1736034.

[43] S. Rühle, Tabulated values of the shockley–queisser limit for single junction solar cells, Solar Energy 130 (2016) 139–147. URL: https://doi.org/10.1016/j.solener.2016.02.015. doi:10.1016/j.solener.2016.02.015.

[44] P. Virtanen, R. Gommers, T. E. Oliphant, M. Haberland, T. Reddy, D. Cournapeau, E. Burovski, P. Peterson, W. Weckesser, J. Bright, S. J. van der Walt, M. Brett, J. Wilson, K. J. Millman, N. Mayorov, A. R. J. Nelson, E. Jones, R. Kern, E. Larson, C. J. Carey, İ. Polat, Y. Feng, E. W. Moore, J. VanderPlas, D. Laxalde, J. Perktold, R. Cimrman, I. Henriksen, E. A. Quintero, C. R. Harris, A. M. Archibald, A. H. Ribeiro, F. Pedregosa, P. van Mulbregt, SciPy 1.0: fundamental algorithms for scientific computing in Python, Nature Methods 17 (2020) 261–272. URL: https://www.nature.com/articles/s41592-019-0686-2. doi:10.1038/s41592-019-0686-2, publisher: Nature Publishing Group.